



Shape-controlled synthesis of BiVO₄ hierarchical structures with unique natural-sunlight-driven photocatalytic activity



Shuying Dong^a, Jinglan Feng^a, Yukun Li^a, Limin Hu^a, Menglin Liu^a, Yifei Wang^b, Yunqing Pi^a, Jingyu Sun^{c,*}, Jianhui Sun^{a, **}

^a School of Environment, Henan Normal University, Key Laboratory for Yellow River and Huai River Water Environmental and Pollution Control, Ministry of Education, Henan Key Laboratory for Environmental Pollution Control, Xinxiang, Henan, 453007, PR China

^b State Key Laboratory of Water Environment Simulation, School of Environment, Beijing Normal University, Beijing 100875, PR China

^c Center for Nanochemistry (CNC), Beijing National Laboratory for Molecular Sciences, College of Chemistry and Molecular Engineering, Peking University, Beijing 100871, PR China

ARTICLE INFO

Article history:

Received 30 October 2013

Received in revised form 15 January 2014

Accepted 19 January 2014

Available online 10 February 2014

Keywords:

BiVO₄

Shape control

Natural sunlight

Photocatalytic

Rhodamine B

ABSTRACT

A detailed study on the shape control of bismuth vanadate (BiVO₄) hierarchical structures and on their corresponding natural sunlight-driven photocatalytic activities was performed. We have developed a time-saving, cost-effective, surfactant-free approach for the controlled synthesis of uniform monoclinic scheelite BiVO₄ hierarchical structures, obtaining diverse BiVO₄ architectures including peanuts, dumbbells, flowers, spheres, olives, and rod-sheaves, *via* facile pH-dictated solvothermal routes with the aid of either NH₃·H₂O or NaOH. The influences of the morphologies of the synthesized BiVO₄ hierarchical structures on the photocatalytic degradation of Rhodamine B (RhB) have been investigated, indicating that the enhanced photocatalytic performances were neither related to the surface area values nor the aspect ratios of the fabricated photocatalysts, but associated with the unique shaped configurations produced under specific low temperature hydrothermal conditions. The effects of the active species involved in the photocatalytic process and the cycle-stability of the prepared BiVO₄ photocatalysts have also been examined.

© 2014 Elsevier B.V. All rights reserved.

1. Introduction

The growing demand for cleaner water environment worldwide has spurred the development of wastewater treatment technologies, which mainly include overland flow system [1], zero-valent iron process [2], hydrodynamic cavitation technology [3], advanced oxidation process [4], and membrane bioreactor system [5] etc. Among these, heterogeneous semiconductor photocatalysis is of intensive usage, enabling facile, efficient, and cost-effective removal of aqueous pollutants, specifically, great efforts have been exerted to develop visible-light responsive photocatalysts [6,7]. The success of photocatalytic reactions greatly depends on the proper selection of catalyst materials. In this regard, bismuth vanadate (BiVO₄) has attracted considerable interest to

date due to its narrow band gap, non-toxicity, high stability, and advanced sunlight-harvesting capacity [8,9]. BiVO₄ can exist in three crystalline phases, namely, tetragonal scheelite, tetragonal zircon, and monoclinic scheelite, where phase transitions may occur between these phases under different thermal conditions [10]. It was reported that tetragonal BiVO₄ with a 2.9 eV band gap mainly possesses an ultraviolet (UV) absorption band, whilst monoclinic BiVO₄ with a 2.4 eV band gap could absorb the solar spectrum up to the blue light region of approx. 520 nm, resulting in the fact that monoclinic scheelite structured BiVO₄ could exhibit far better visible-light-driven photocatalytic performance over the other crystal forms [11,12].

It is well known that the photocatalytic activities of nanostructured catalysts strongly rely on their sizes and shapes due to the morphology–property relationship at the nanoscale [13–16]. Latest efforts have been made to achieve controllable synthesis of BiVO₄ hierarchical nanostructures for enhanced photocatalytic performances [16–20]. For instance, Ressnig et al. employed dimethyl methylphosphonate as the surfactant to tailor the synthesis of hierarchically structured BiVO₄ architectures and found out that

* Corresponding author. Tel.: +86 10 62757157.

** Corresponding author at: Henan Normal University, School of Environment, No. 46, Jianshe Road, Henan, Xinxiang 453007, PR China. Tel.: +86 373 332 5971.

E-mail addresses: sunjy-cnc@pku.edu.cn (J.Y. Sun), sunjh@htu.cn (J.H. Sun).

BiVO_4 nanoplatelets (synthesized at pH 4) exhibited superior optimal activity in both organic dye degradation and water oxidation [18]. Obregon et al. reported the formation of various shaped monoclinic BiVO_4 materials by means of a surfactant free hydrothermal method, and the best photocatalytic performance was attained by the samples with needle-like morphologies [19]. Tan and colleagues obtained different shaped BiVO_4 powders with distinct photocatalytic performances by tuning the pH conditions during the microwave-assisted hydrothermal synthesis [20]. Despite the fact that research has been flourished into the field of BiVO_4 photocatalysis for such a long period, thorough studies with regard to the influences of delicate morphological control upon the photocatalytic response and photodegradation mechanism have still been limited [21]. Furthermore, there have been few reports on employing natural sunlight as the light source for studying the BiVO_4 photocatalytic properties, thus detailed study concerning these aspects for the BiVO_4 photocatalysts becomes quite imperative.

Herein, we report a time-saving, cost-effective, surfactant-free method for the controllable synthesis of uniform BiVO_4 hierarchical structures with distinct shapes. Diverse BiVO_4 architectures, including peanuts, dumbbells, flowers, spheres, olives, and rodsheaves, have been fabricated via facile pH-dictated solvothermal processes. The morphology evolution of the BiVO_4 hierarchical structures has been extensively investigated, based on the electron microscopy observation. The influences of the morphologies of the synthesized BiVO_4 hierarchical structures on the photocatalytic degradation of Rhodamine B (RhB) have been studied. Probing into the active species involved in the photocatalytic process and the cycle-stability of the prepared BiVO_4 photocatalyst have also been conducted. This study provides an in-detail investigation on the effects of delicate morphology-control of BiVO_4 hierarchical structures upon the natural sunlight-driven photocatalytic activity.

2. Experimental

2.1. Synthesis of BiVO_4 photocatalysts

All the chemicals were analytical grade reagents and used as received without further purification. Deionized water was used throughout this study.

In a typical synthesis procedure, 0.97 g $\text{Bi}(\text{NO}_3)_3 \cdot 5\text{H}_2\text{O}$ was dissolved in a 50 mL mixed solution of $\text{C}_2\text{H}_5\text{OH}:\text{CH}_3\text{COOH}:\text{H}_2\text{O} = 1:1:3$ (v:v:v) by vigorous stirring for 20 min, the prepared solution was marked as solution X. Meanwhile, 0.23 g NH_4VO_3 was dissolved in a 20 mL ammonia solution ($\text{NH}_3 \cdot \text{H}_2\text{O}:\text{H}_2\text{O} = 3:1$, v:v) or a NaOH solution (5 M) by vigorous stirring for 20 min, and the resultant solution was marked as solution Y. Then Y was added into X at room temperature under continuous stirring for 30 min until it became homogeneous, and the pH value of the mixture was correspondingly adjusted by $\text{NH}_3 \cdot \text{H}_2\text{O}$ or NaOH. The obtained mixture was consequently transferred into a teflon-lined stainless steel autoclave, where it was heated under autogenous pressure at designed temperatures for requested periods. After the heating, the autoclave was naturally cooled down to room temperature. The yellow precipitate was then collected by filtration, washed by deionized water and ethanol, and dried at 80 °C in an oven overnight.

In order to name the sample, the capital letter 'A' or 'S' has been used to distinguish the alkaline solution employed during the sample preparation (ammonia or sodium hydroxide), for example, A-BiVO_4 in general refers to the sample prepared by using $\text{NH}_3 \cdot \text{H}_2\text{O}$. More specifically, pH value of the mixed solution (precursor) during synthesis could be indicated (i.e. S6.26 particularly refers to the

sample synthesized by using NaOH at pH value of 6.26). However, there was an exception that the sample with the pH value of the precursor at pH 1.7 was synthesized without any involvement of $\text{NH}_3 \cdot \text{H}_2\text{O}$ or NaOH.

2.2. Characterizations

The crystal phase of the prepared BiVO_4 hierarchical structures was analyzed by X-ray diffraction (XRD). The patterns were recorded in the 2θ range of 10–70° with a scan rate of 0.02°/0.4 s using a Bruker-D8-AXS diffractometer system equipped with a Cu $\text{K}\alpha$ radiation ($\lambda = 0.15406 \text{ \AA}$) (Bruker Co., Germany). The morphologies of obtained materials were inspected by using a JSM-6390LV scanning electron microscopy (SEM) and a JEM-2100 high-resolution transmission electron microscopy (HRTEM). Fourier transform infrared (FT-IR) spectra were recorded using a FTIR Analyzer (Perkin-Elmer, Spectrum 400), and the KBr was served as a reference sample. The measurements of low-temperature N_2 adsorption were carried out by using a Micromeritics ASAP 2020 apparatus operating at -196°C , where all the samples were degassed at 100°C for 6 h prior to the measurement. The Ultraviolet-visible (UV-Vis) diffuse reflectance spectra were obtained with the aid of a UV-Vis-NIR spectrophotometer (Lambda 950, PerkinElmer) by using BaSO_4 as a reference, where the spectra were recorded at the wavelength range of 300–800 nm. The photoluminescence (PL) spectra of photocatalysts were recorded using a Fluorescence Spectrophotometer (FP-6500, Japan) equipped with a Xenon lamp at an excitation wavelength of 325 nm.

2.3. Evaluation of natural sunlight photocatalytic activity

The photocatalytic activities of the as-obtained BiVO_4 materials were monitored through the photodegradation of RhB under natural sunlight irradiation. Photocatalytic reactions were carried out in a 250 mL borosilicate photochemical batch reactor. To ensure the sufficient illumination of the natural sunlight, all photocatalytic experiments were intentionally performed between 8:10 a.m. and 6:10 p.m. (the reaction time was 10 h) on those sunny days during the summer 2013. The ambient temperature was between 29 °C and 34 °C. The time-dependent light density of the natural sunlight was measured by using a digital Lux meter (UA1010B, Shenzhen UYIGAO E&T Co., China) during our experiments, where the average time-dependent illuminations of the natural sunlight were obtained as follows: 24,000, 64,000, 80,000, 71,000, 45,000, and 10,000 lx for 8:10 a.m., 10:10 a.m., 12:10 p.m., 2:10 p.m., 4:10 p.m., and 6:10 p.m., respectively. In all experiments, the catalyst (0.10 g) were added to 200 mL RhB aqueous solution (5 mg/L). No pH adjustment was used during the entire course of the photodegradation process. Prior to irradiation, the suspension was magnetically stirred (300 rpm) in the dark for 40 min, in order to achieve an adsorption-desorption equilibrium between the RhB molecules and catalyst particles. During each photocatalytic experiment, 2 mL of the suspension was collected at predetermined time intervals for analysis.

The concentration of RhB was analyzed by measuring the absorption intensity at its maximum absorbance wavelength of $\lambda = 553 \text{ nm}$ using a UV-Vis spectrophotometer (UV-1700, SHIMADU) with a 1 cm path length spectrometric quartz cell, and was calculated from the calibration curve. The degradation efficiency of the RhB dye wastewater was determined according to the following equation:

$$\text{degradation efficiency}(\%) = \frac{C_0 - C_t}{C_0} \times 100\% \quad (1)$$

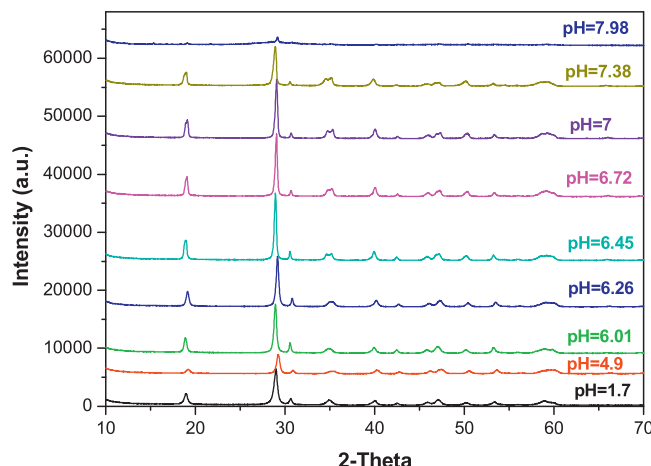


Fig. 1. XRD patterns of BiVO_4 samples prepared by hydrothermal treatment at 80°C for 3 h using $\text{NH}_3\cdot\text{H}_2\text{O}$ as the pH controlling agent.

where C_0 was the initial concentration of RhB (after the standing in the dark for 40 min) and C_t was the concentration of RhB at certain reaction time t .

2.4. Evaluation of simulated sunlight photocatalytic activity

The photocatalytic activities of the as-obtained BiVO_4 materials were also evaluated through the photodegradation of colorless sulfanilamide under simulated sunlight irradiation. A 300 W U-shaped xenon lamp was used as the light source (Yaming Company, Shanghai) and the irradiation time was 60 min. The temperature of the reactions was maintained at room temperature with the aid of a water circulation system. 0.1 g A6.26 or S6.26 was added into 200 mL sulfanilamide solution with a concentration of 15 mg/L. Other experimental apparatus and procedures employed were identical to that described in Section 2.3.

3. Results and discussion

3.1. Tailoring the shapes of BiVO_4 hierarchical structures with the aid of $\text{NH}_3\cdot\text{H}_2\text{O}$

Fig. 1 shows the XRD patterns of BiVO_4 samples prepared through low temperature hydrothermal treatments at 80°C for 3 h using $\text{NH}_3\cdot\text{H}_2\text{O}$ as pH controlling agent. The diffraction peaks of samples (when $\text{pH} \leq 7.38$) can be easily indexed to a pure monoclinic scheelite BiVO_4 phase, which are in good agreement with the reference data (JCPDS No. 14-0688). It is worth-noting that the relative intensities of the diffraction peaks (I_{110}/I_{040}) increase with the increasing pH value of the precursor, indicating that (110) facets became dominated over (040) facets in response to the decrease of acidity of the precursor. However, when the pH reached 7.98 by adding $\text{NH}_3\cdot\text{H}_2\text{O}$, the diffraction peaks of monoclinic scheelite BiVO_4 suddenly vanish. The XRD analysis reveals that structural evolutions of synthesized BiVO_4 samples might occur during the course of pH-dictating process with the aid of $\text{NH}_3\cdot\text{H}_2\text{O}$.

The diversified morphologies of the BiVO_4 architectures synthesized with the aid of $\text{NH}_3\cdot\text{H}_2\text{O}$ were examined by SEM, as depicted in **Fig. 2**. **Fig. 2a** shows that the sample produced at pH 1.7 is composed of a mixture of disordered microclusters with no predominant shape observed. With the adjustment of pH value of the precursor up to 4.9, uniform peanut-shaped particles (A4.9) were formed (**Fig. 2b**), where the reason for the product uniformity is probably due to the fact that the addition of $\text{NH}_3\cdot\text{H}_2\text{O}$ promoted the formation of acetamide, a solubilizer that could increase the

dispersion of the precursor and hence assist the shape-selective synthesis [22]. As the pH value was manipulated to reach 6.01, A6.01 sample with a dumbbell-shaped structure can be fabricated (**Fig. 2c**). Moreover, fine dumbbells (A6.26) were uniformly displayed as the pH rose to 6.26 (**Fig. 2d**). However, slightly increasing the pH value led to the distortion of the shape of these dumbbells, where flower-like morphologies are formed as shown in the SEM micrographs (**Fig. 2e–g**). At pH 7.38, the flowers collapsed into needle-like branches (**Fig. 2h**), and final tuning the pH value to reach 7.98 resulted in the formation of pieces of chunk clusters with no defined shape (**Fig. 2i**).

A key feature of the grown BiVO_4 materials as shown in the current study is the pH dictated, quick responded shape evolution with the addition of $\text{NH}_3\cdot\text{H}_2\text{O}$. In order to attain detailed information on the microstructures of these shaped BiVO_4 , TEM characterization was performed on the as-synthesized product. **Fig. 3a, c, e, g, and i** displays general views of the BiVO_4 samples prepared with $\text{NH}_3\cdot\text{H}_2\text{O}$ at different pH values, namely A4.9, A6.26, A6.72, A7, and A7.38. The shape of these samples ranges from peanut, dumbbell, flower, to rod-sheave corresponding to the SEM observation shown in **Fig. 2**, with a measured mean length at approx. 1.5 μm , 3 μm , 5 μm , 15 μm and 1.3 μm , respectively. The aspect ratio was calculated from the mean length divided by the maximum width of the individual structure, which was approx. 1.75, 1.25, 2.82, 1.29, and 7.11 for the sample of A4.9, A6.26, A6.72, A7, and A7.38, respectively. **Fig. 3b, d, f and h** are the representative HRTEM images of the A4.9, A6.26, A6.72, and A7 samples. The clear lattice fringes presented in each image are indicative of high crystallinity. The d-spacings were measured to be 0.475 nm for all the samples, which are in good agreement with the lattice spacings of (110) of monoclinic scheelite BiVO_4 . The TEM results are consistent with the information extracted from the XRD patterns, stating that the sample was experiencing morphological changes during the course of pH dictating synthesis so that (110) plane eventually became the preferential orientation at higher pH. Such trend has recently been observed by Obregon et al. [19], but our study offers more delicate control during synthesis over shape evolution of monoclinic scheelite BiVO_4 to achieve better shape selectivity and enhanced product quality in a shorter range of pH tunes.

To gain further understanding toward the shape evolution of the BiVO_4 hierarchical architectures, time-dependent investigations were carried out by extracting products at different reaction stages. Specifically, hydrothermal formation of BiVO_4 at pH 6.26 (adjusted via $\text{NH}_3\cdot\text{H}_2\text{O}$) was sampled at different reaction timeslots, namely 20 min, 40 min, 60 min, 120 min, and 360 min. **Fig. S1** (see the Supporting information) displays the SEM observations of the morphological evolution of the reaction products. A typical hydrothermal ripening process known as Ostwald ripening can be applied here to describe the formation of dumbbell-like BiVO_4 hierarchical architectures [23]. At the beginning, the direct mixing of the two solutions (X and Y) led to the formation of amorphous particles with random size distributions (**Fig. S1a**). Under hydrothermal treatment, the formation of tiny crystalline nuclei in a supersaturated medium marked the beginning of BiVO_4 crystal growth. In the earlier 40 min reaction (**Fig. S1b and c**), larger pieces eventually transformed to smaller particles, however, with the course of the reaction, Ostwald ripening process became dominating, leading to the agglomeration of small particles to form well-crystallized structures [24]. At 60 min reaction time, the intermediate samples show the coexistence of irregular dumbbell structures and particles (**Fig. S1d**). Further increasing the hydrothermal time to 120 min gave rise to the formation of uniform dumbbell structures, where the irregular particles vanished, suggesting that the dumbbell shapes were grown at the cost of the smaller particles (**Fig. S1e**). Prolonged reaction time of 360 min exerted no effect on the shape evolution of the A6.26 samples (**Fig. S1f**).

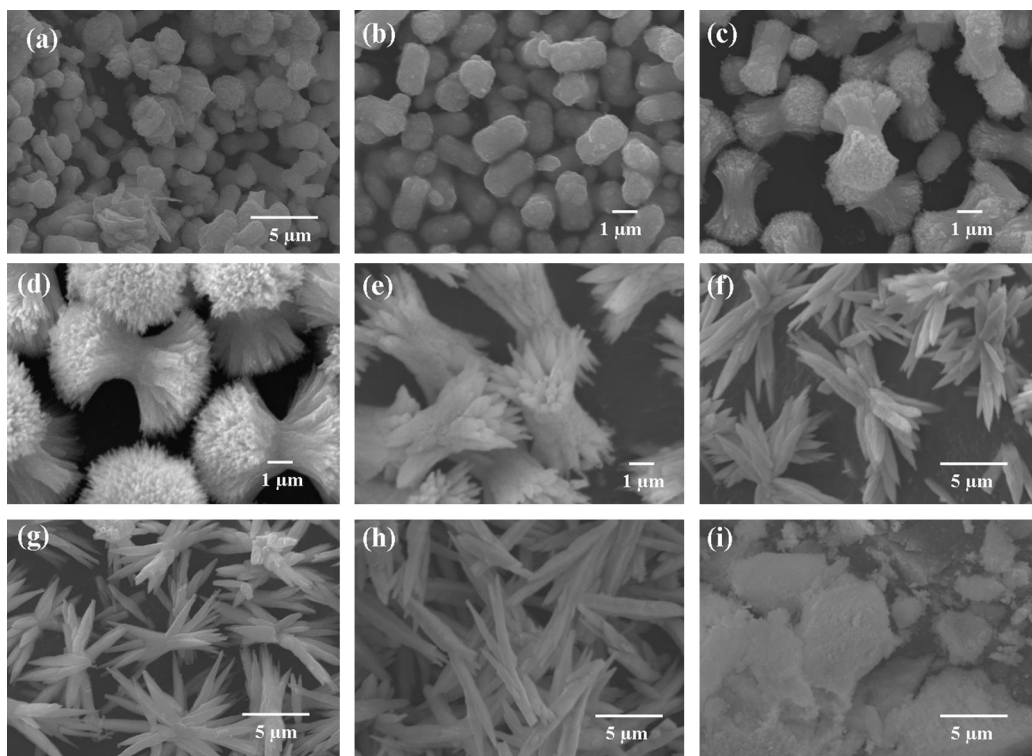


Fig. 2. SEM images of different shaped BiVO₄ hierarchical structures obtained by varying the pH values of the precursors using NH₃·H₂O as the pH controlling agent. (a) pH = 1.7; (b) pH = 4.9; (c) pH = 6.01; (d) pH = 6.26; (e) pH = 6.45; (f) pH = 6.72; (g) pH = 7; (h) pH = 7.38; (i) pH = 7.98.

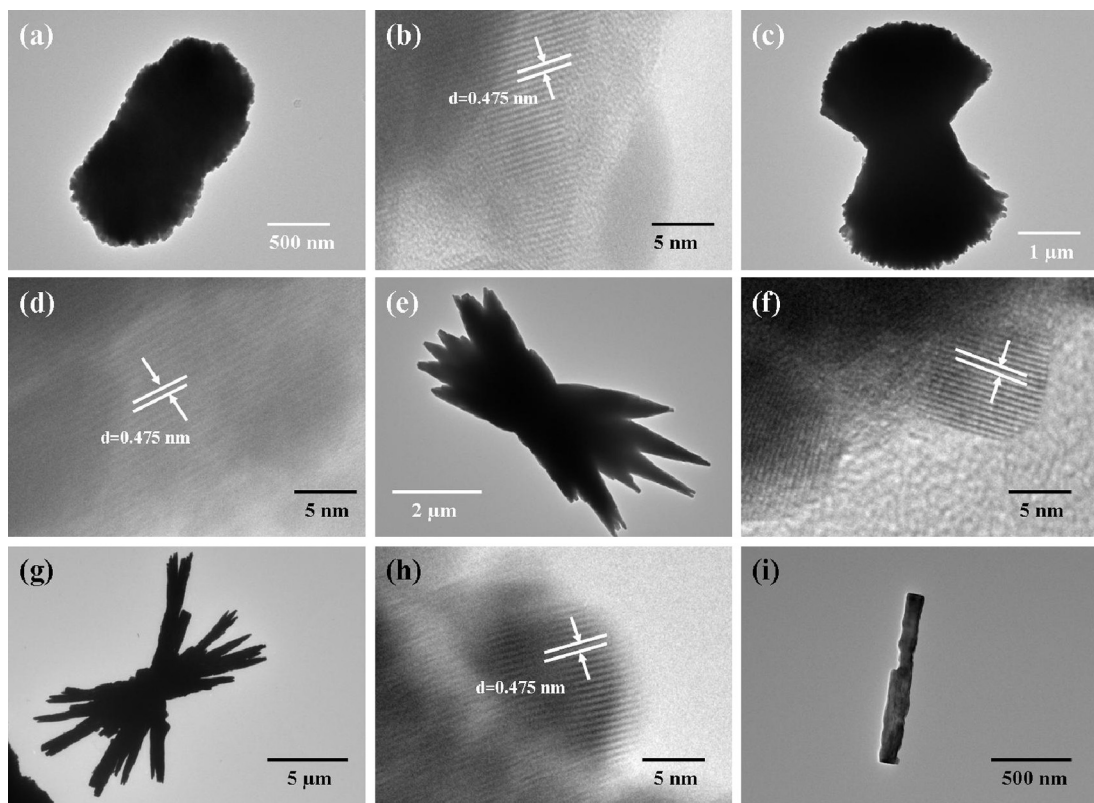


Fig. 3. Representative TEM micrographs of different shaped BiVO₄ hierarchical structures obtained by varying the pH values of the precursors using NH₃·H₂O as the pH controlling agent. (a–b) pH = 4.9; (c–d) pH = 6.26; (e–f) pH = 6.72; (g–h) pH = 7; (i) pH = 7.38.

Further XRD analysis on the A6.26 samples from the time-dependent investigations is in good agreement with the SEM characterization, as shown in Fig. S2. Prior to the hydrothermal reaction, the precursor displays no apparent peak (black curve); however, the monoclinic scheelite BiVO_4 crystalline phase quickly appears at 20 min hydrothermal treatment (red curve), after which the XRD patterns of the sampling remain unchanged with regard to the reaction time. No additional phase can be detected in the whole course of the reaction, even that the hydrothermal time was prolonged to 360 min (magenta curve).

3.2. Tailoring the shapes of BiVO_4 hierarchical structures with the aid of NaOH

Interest in using NaOH as a reagent or pH controller for the hydrothermal synthesis of BiVO_4 stems from the fact that the involvement of NaOH could lead to the generation of various shaped BiVO_4 structures [25–27]. In our case, the use of NaOH as the pH controller enables expansion of the shape diversity of synthesized BiVO_4 hierarchical structures. Moreover, it is meaningful to compare the structural and photocatalytic information of A- BiVO_4 and S- BiVO_4 produced by using $\text{NH}_3\cdot\text{H}_2\text{O}$ (weak base) and NaOH

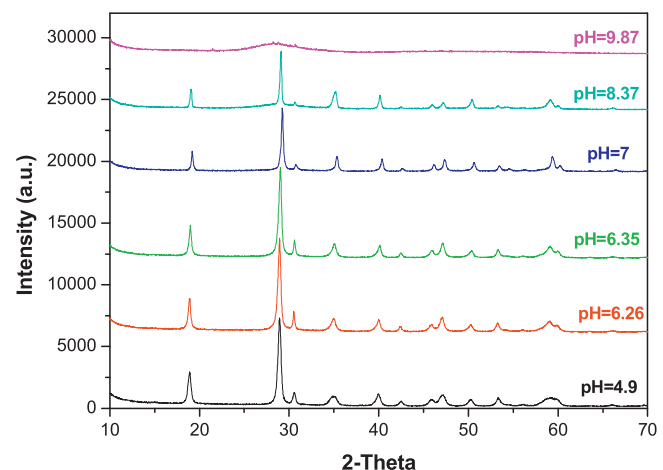


Fig. 4. XRD patterns of BiVO_4 samples prepared by hydrothermal treatment at 80°C for 3 h using NaOH as the pH controlling agent.

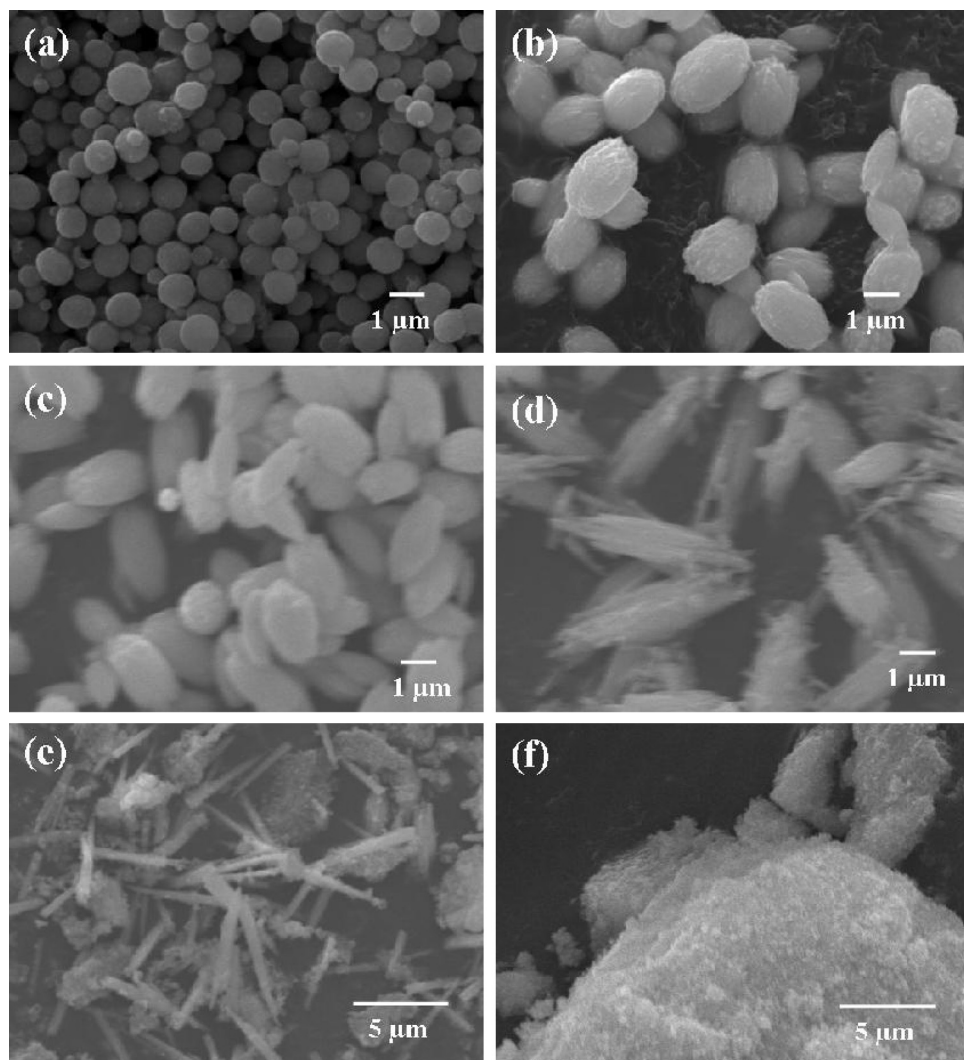


Fig. 5. SEM images of different shaped BiVO_4 hierarchical structures obtained by varying the pH values of the precursors using NaOH as the pH controlling agent. (a) pH = 4.9; (b) pH = 6.26; (c) pH = 6.35; (d) pH = 7; (e) pH = 8.37; (f) pH = 9.87.

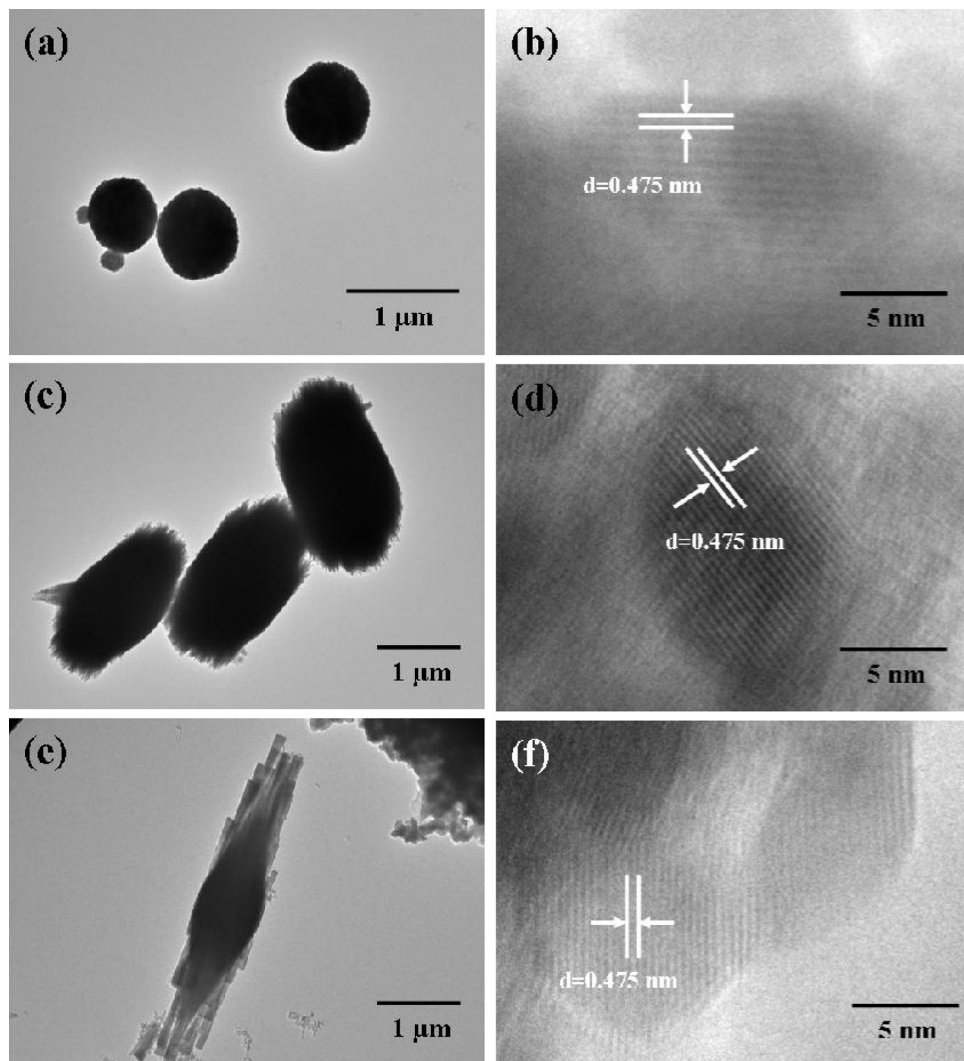


Fig. 6. Representative TEM micrographs of different shaped BiVO_4 hierarchical structures obtained by varying the pH values of the precursors using NaOH as the pH controlling agent. (a–b) pH = 4.9; (c–d) pH = 6.26; (e–f) pH = 7.

(strong base), respectively. Fig. 4 shows the XRD patterns of BiVO_4 samples prepared by the hydrothermal treatment at different pH values of precursors using NaOH as the pH controller. Accordingly, the diffraction peaks of samples (when $\text{pH} < 9.87$) can be indexed to a pure monoclinic scheelite BiVO_4 phase, whereas the S9.87 sample displays no sharp diffraction peak. The morphologies of the grown products were examined by SEM and TEM. Fig. 5 displays the SEM observations of S- BiVO_4 samples, where the overall microstructures of S- BiVO_4 are quite different from that of A- BiVO_4 . At pH 4.9 microspheres can be observed (Fig. 5a). As the pH value was adjusted to 6.26, the elongation of microspheres gave rise to the formation of olive-like particles (Fig. 5b). Slightly increasing the pH value to 6.35 tended to flatten the olive-shaped particles, as shown in Fig. 5c. When the pH value was increased to 7, all these olives were further extended to form the rod-sheaf structures (Fig. 5d). Further tuning the pH value to 8.37 led to the breakage of the rod-sheaves into a mixture of single rods and big particles (Fig. 5e). Final increase the pH value to 9.87 resulted in the formation of amorphous lumps instead of rod-like structures (Fig. 5f).

Fig. 6 displays the TEM characterization of the BiVO_4 samples (S- BiVO_4) prepared by using NaOH as the pH controller. Fig. 6a, c, and e show general views of S4.9, S6.26, and S7, with a structure of

sphere, olive, rod-sheaf and a corresponding aspect ratio at approx. 1.05, 1.84, and 3.96, respectively. The TEM characterization of the particle shapes is consistent with the SEM observations shown in Fig. 5. Fig. 6b, d, and f are the representative HRTEM micrographs of S4.9, S6.26, and S7, respectively. Likewise, the d-spacings were measured to be 0.475 nm for all the samples, which agree well with the lattice spacings of (1 1 0) of monoclinic scheelite BiVO_4 .

3.3. Discussing the formation of different shapes of BiVO_4 hierarchical structures

The mechanisms of the shape evolution and the exact influences of the pH values on the shape control are complex and thus remain not that easy to disclose. On a basis of our obtained results, we speculate that the shape/morphology of the product depends upon the competition between the nucleation and growth rates during the crystal formation. Briefly, at a low pH, the hydrolyzation of $\text{Bi}(\text{NO}_3)_3 \cdot 5\text{H}_2\text{O}$ was inhibited, leading to the fact that more H^+ species were liberated and a tiny amounts of BiVO_4 were formed, and hence there were fewer crystal nuclei [28]. When the pH value of the precursor was increased by adding $\text{NH}_3 \cdot \text{H}_2\text{O}$ or NaOH, the nucleation rate and crystal growth rate of BiVO_4 can be adjusted via a dissolution–recrystallization process [29]. With the increase

of the alkali concentration in the system, the solution reached a saturated level, which accelerated the crystal growth rate. Since the growth rate of the (110) facets was greater than that of the (040) facets, as the reaction proceeded, the crystals grew along the different directions at distinct growth rates, resulting in the morphology evolution. Further increase in crystal growth rates of the primary particles at higher pH gave rise to highly anisotropic particle growth, owing to the blockage induced by OH^- ions attracted on the particle surface [20]. Therefore, when the pH increased over a critical value, the hierarchical structure collapsed.

The microscopic observation in this study has indicated that the BiVO_4 hierarchical structures tended to elongate along the *b* axis in the (110) planes with the increase of pH values of precursors. However, it is noted that the morphologies of BiVO_4 hierarchical structures synthesized under same pH values are quite different for the two series (*i.e.* A6.26 and S6.26). To identify the causes of this phenomenon, we have examined the FT-IR spectra of A6.26 and S6.26, which was inspired by the investigation performed by Gotic et al. on reporting that the morphologies of synthesized product had a crucial effect on the positions of IR bands [30].

Fig. S3 shows FT-IR spectra of A6.26 and S6.26 samples collected at different hydrothermal reaction timeslots. The spectrum of sample precursor of A6.26 is characterized by a very broad and strong IR band at 729 cm^{-1} and shifts to 741 cm^{-1} with prolonging hydrothermal periods. As for S6.26, the broad and strong band is located at 750 cm^{-1} , which shows no apparent shift prior to (the precursor) and after hydrothermal treatment. These bands at $700\text{--}800\text{ cm}^{-1}$ can be attributed to the bending vibration of the VO_4^{3-} [31]. The IR band at around 2440 cm^{-1} in A6.26 corresponds to the vibrations of adsorbed CO_2 molecules, which disappears after hydrothermal reaction for 3 h (blue curve), indicating that thorough treatment led to the complete removal of surface-attached CO_2 molecules. Interestingly, this band has not been observed for the sample of S6.26 throughout the whole process of reaction. Another two detected peaks lay in the bands at 1637 cm^{-1} and at $3320\text{--}3460\text{ cm}^{-1}$, which correspond to the vibration of adsorbed H_2O molecules and surface OH^- groups, respectively [31–34]. Apparently, the peaks of the two bands for S6.26 are stronger than those of A6.26, revealing that S6.26 possesses more surface adsorbed H_2O molecules and OH^- groups than A6.26. It is known that the surface adsorbed H_2O molecules and OH^- groups are critical for the photocatalytic reactions, since they may react with photogenerated h^+ on the catalyst surface to produce OH^\bullet radicals [35]. The difference in the FT-IR spectra for the samples of A6.26 and S6.26 is indicative of differences in the sample structures, formation pathways, as well as photocatalytic properties.

3.4. Measuring the photochemical properties of the synthesized BiVO_4 hierarchical structures

The photoluminescence (PL) is a facile technique to study the photochemical properties of semiconductor materials, where the PL emission mainly originates from the recombination of the excited electrons and holes [36]. Fig. 7 shows the PL spectra of the synthesized A- BiVO_4 and S- BiVO_4 . It can be observed that all the samples (both A- and S-series) exhibit evident PL signals with similar curve shapes, revealing that the modification in the synthesized BiVO_4 morphologies did not induce new PL signals. Both series of samples possess strong PL peaks centering at approx. 525 nm, which originates from the recombination of the hole formed from the hybrid orbitals of Bi 6s and O 2p (valence band (VB)) and the electron generated from the V 3d orbitals (conduction band (CB)) [37]. Also, it has been reported that the higher peak intensity indicated the bigger probability of charge carrier recombination [38]. By taking A6.26 and S6.26 as representatives, one can observe from Fig. 7 that the PL emission intensity of A6.26 stays stronger than that

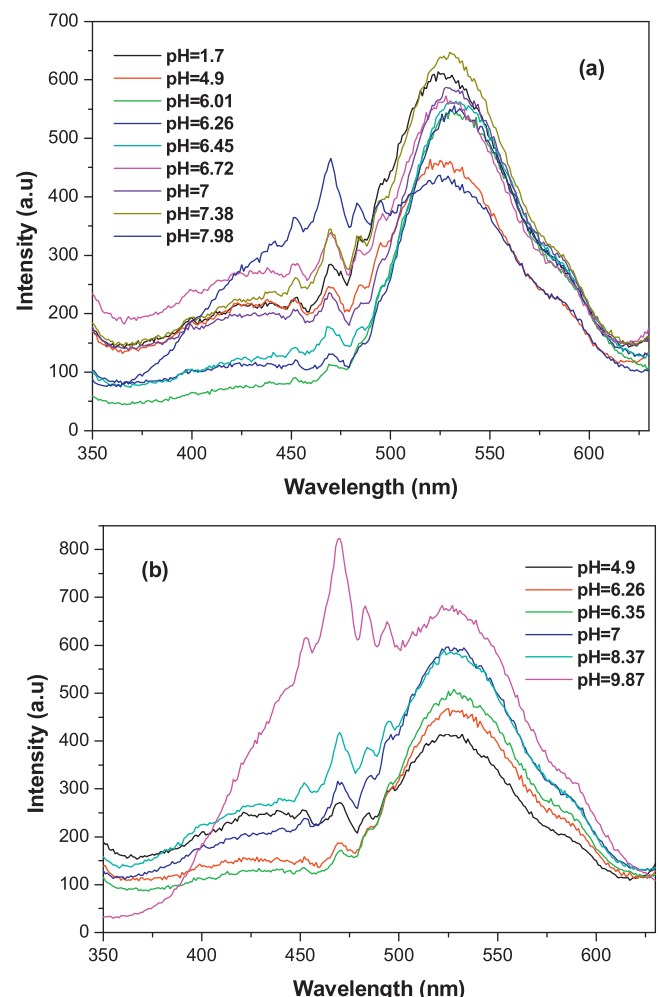


Fig. 7. Room temperature PL spectra of (a) A- BiVO_4 and (b) S- BiVO_4 samples prepared at different pH values of the precursors.

of S6.26, revealing that the retarded recombination rates between the photoinduced holes and electrons occurred in the S6.26 sample compared to that of the A6.26 sample, which could lead to an enhanced photocatalytic activity.

The optical absorption property of the semiconductor has been recognized as the key factor in affecting its photocatalytic performance [37]. Fig. 8 shows the UV-Vis diffuse-reflectance spectra of the well-shaped BiVO_4 hierarchical structures synthesized at different pH values of precursors. Both the A- BiVO_4 (Fig. 8a) and S- BiVO_4 (Fig. 8c) exhibit a strong absorption in the UV-Visible light region. The steep shapes of all the spectra indicate that the visible-light absorption were not due to the transition from impurity levels but the band-gap transition. It is worth-noting that the absorption edges for both the A- BiVO_4 and S- BiVO_4 samples blue shift eventually as the pH values of the precursors increase. As for A- BiVO_4 , the absorption edge is measured to be at approx. 580 nm (pH 1.7), 560 nm (pH 4.9), 555 nm (pH 6.26), and 540 nm (pH 7); the same trend could also be found with regard to the S- BiVO_4 sample. This phenomenon was also observed by Yu et al. [21]. From our microscopic observations it is easy to notice that the particle sizes of the sample are far beyond the region (*i.e.* $<7\text{ nm}$) where the quantum size effects can be applied, in this regard, variations in the morphological and electronic structures might account for the blue shift of the sample absorption edges [39,40]. Besides, in particular for A6.26, the absorption in the wavelength range of 300–500 nm is the most prominent amongst the samples, which could be ascribed

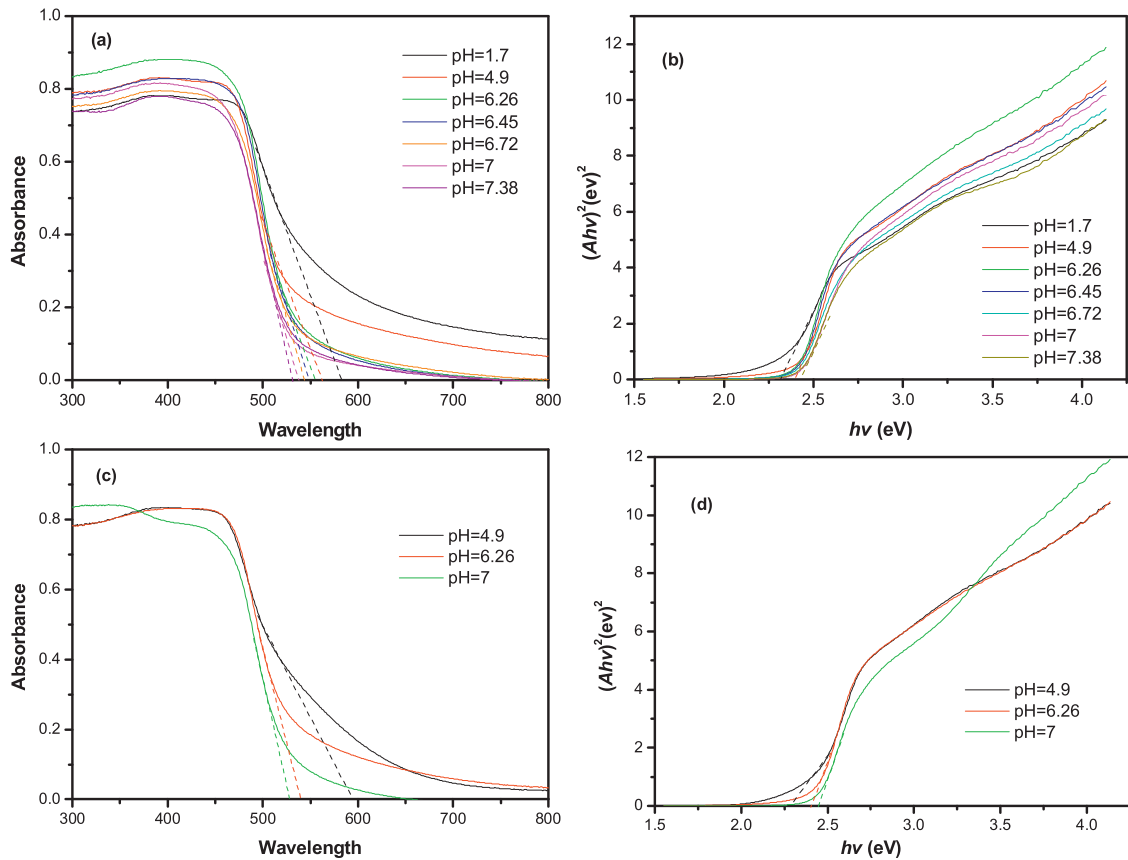


Fig. 8. UV-Vis diffusion reflectance spectra of (a) A-BiVO₄ and (c) S-BiVO₄ samples. The relationship between $(Ahv)^2$ and the photon energy ($h\nu$) of (b) A-BiVO₄ and (d) S-BiVO₄ samples is indicative of the band-gap of synthesized materials.

to the unique configuration of the A6.26 sample (A-BiVO₄ forms perfectly dumbbell shaped-structure with uniform size distributions at pH 6.26). It is also interesting to note that the inconsistency between the results of the UV-Vis and PL measurements, where the blue shift of the band gap energies is observed in Fig. 8 whilst the PL peak positions remain unchanged in Fig. 7. This phenomenon is quite universal and could be suggested to be induced by the morphological changes of the investigated materials (in this case, BiVO₄), which contributes to the blue shift of absorption edges as well as the variations in the PL emission intensities rather than the PL peak positions, as reported in some other photocatalytic systems [41–43].

Moreover, the energy band structures of a semiconductor stay important in determining its photocatalytic activity. The relationship of absorbance and incident photon energy $h\nu$ can be described as Eq. (2).

$$Ahv = C(hv - E_g)^{1/2} \quad (2)$$

where A , E_g , h and ν represent the absorption coefficient, the band-gap energy, Planck constant, and the incident light frequency, respectively, and C denotes a constant. The band-gap energy (E_g) of the obtained BiVO₄ can therefore be estimated from a plot depicting $(Ahv)^2$ versus $h\nu$. The intercept of the tangent to the X axis gives rise to a good approximation of the band-gap energy for the obtained A-BiVO₄ (Fig. 8b) and S-BiVO₄ (Fig. 8d). The estimated band-gap energies of A1.7, A4.9, A6.26, and A7 were to be approx. 2.34, 2.40, 2.43, and 2.45 eV, respectively, whereas for S-BiVO₄, the band-gap energies were measured to be approx. 2.28 eV (S4.9), 2.40 eV (S6.26), and 2.45 eV (S7). These data are consistent with

the band-gap values of monoclinic scheelite BiVO₄ reported in literature [44] and clearly demonstrate that the electronic structures of BiVO₄ altered along with the pH values of the precursors. A systematic study to understand the reason of the band gap transition along with the change of pH is still ongoing. At lower pH values, the free Bi³⁺ ions were sufficient in the precursor solutions, leading to the generation of small-sized crystals (e.g. S4.9) possessing large density of Bi_{6s} electrons. It was claimed, for the case of monoclinic scheelite BiVO₄, that the presence of Bi_{6s} in the top of the VB results in a more negative energy level of the VB and then a decrease in the band gap [36], this could be the reason why the band-gap values was declining herein with the decrease of pH values of the precursors.

3.5. Investigating the photocatalytic activities of the morphologically controlled BiVO₄ hierarchical structures

3.5.1. Studying the photocatalytic activities, recycle performances, and main oxidative species in terms of natural sunlight-driven degradation of RhB

The photocatalytic performances of both A-BiVO₄ and S-BiVO₄ were examined in terms of degradation of RhB in an aqueous solution under natural sunlight irradiation, as shown in Fig. 9. Within the string of A-BiVO₄ samples hydrothermally synthesized with the aid of NH₃·H₂O, A6.26 exhibited the best degradation efficiency of RhB at 89% after 10 h of sunlight irradiation (blue curve in Fig. 9a). Surprisingly, as for the series of S-BiVO₄ samples hydrothermally synthesized with the aid of NaOH, S6.26 also displayed superior RhB degradation efficiency of 97% (red curve

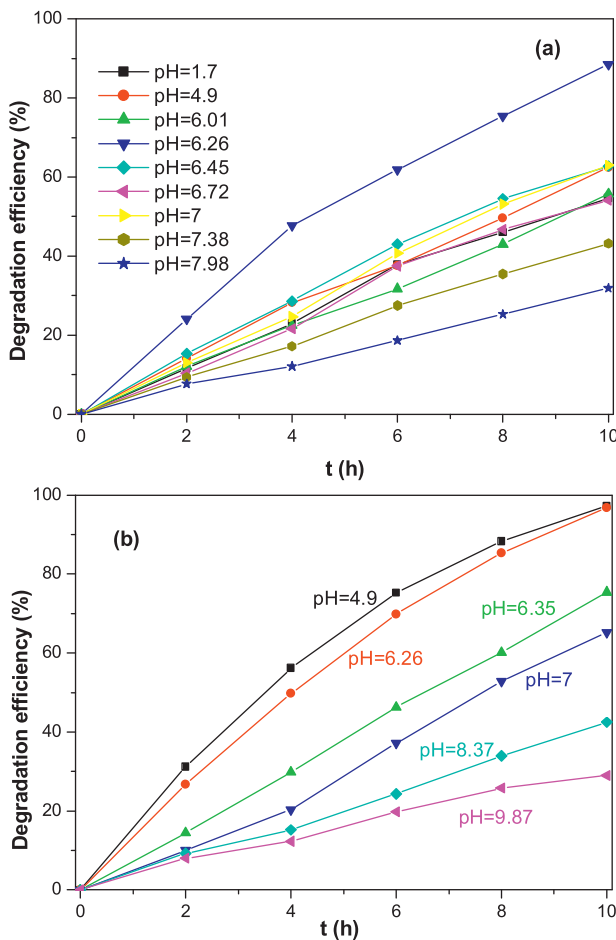


Fig. 9. Photocatalytic degradation of RhB under natural sunlight irradiation over (a) A-BiVO₄ and (b) S-BiVO₄ samples prepared at different pH values of the precursors. (For interpretation of the references to color in this figure legend, the reader is referred to the web version of this article.)

in Fig. 9b), where S4.9 exhibited the similar degradation activity (black curve in Fig. 9b). Furthermore, it is interesting to note that in either scenario, the amorphous BiVO₄ samples of A7.98 and S9.87 without forming stable shapes gave the lowest degradation rate of RhB at 31% and 27%, respectively. The obtained results of the photocatalysis tests suggest that the local structure, crystallinity, and morphological shapes of the synthesized BiVO₄ product.

The recycle experiments were performed to evaluate the photostability of synthesized A6.26 and S6.26 photocatalysts under natural sunlight irradiation. The degradation efficiency of RhB during each cycle (at the duration of 10 h) is shown in Fig. 10. It can be observed that after five cycling runs of photodegradation of RhB, the photocatalytic capacity of either the A6.26 (Fig. 10a) or S6.26 (Fig. 10b) have not exhibited any significant loss. Moreover, the A6.26 and S6.26 photocatalysts employed in the recycle tests were under microscopic and spectroscopic characterizations before and after the experiments. The corresponding SEM micrographs (Fig. S4a and b) and FT-IR spectra (Fig. S4c) reveal that there was no observable change in the morphological shapes as well as the crystal structures of the catalysts. These results suggest that the prepared BiVO₄ has excellent stability and tends not to suffer from photocorrosion during the degradation process.

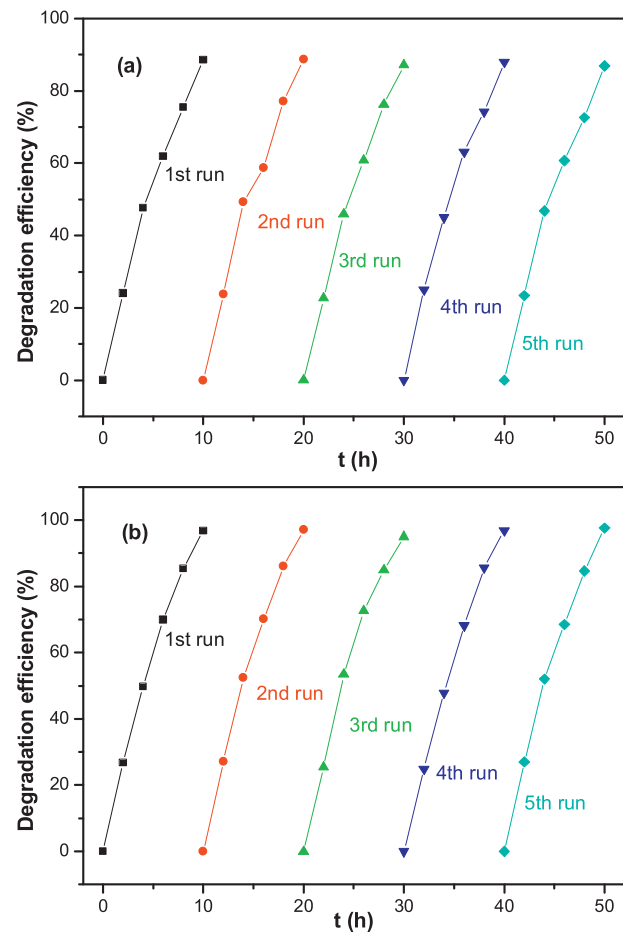


Fig. 10. Photo-stability tests over (a) A6.26 and (b) S6.26 photocatalysts for the cycling photodegradation of RhB under natural sunlight irradiation.

It is of paramount importance to detect main active species in the photocatalytic reaction for elucidating the photocatalytic mechanism of synthesized BiVO₄ hierarchical structures, where the detection can be realized through trapping experiments of oxidative species such as •OH, h⁺, and •O₂[−] by using isopropanol (IPA) (•OH scavenger), ethylene diamine tetraacetic acid (EDTA) (h⁺ scavenger), methyl alcohol (MeOH) (•O₂[−] scavenger), and potassium iodide (KI) (•OH and h⁺ scavenger), respectively. With regard to the A6.26 system, the addition of IPA or MeOH induces a small change in the photocatalytic degradation efficiencies of RhB under the natural sunlight irradiation, as shown in Fig. 11a. However, the photocatalytic activity of A6.26 could be greatly suppressed by the addition of an h⁺ scavenger (EDTA). The results suggest that the photogenerated holes are the dominant oxidative species of A6.26 system, where the •OH and •O₂[−] radicals play an assistant role in the natural sunlight-driven degradation of RhB. From Fig. 11b, it can be seen that in S6.26 system, the photocatalytic activity is also greatly impeded by the dosage of EDTA, revealing that the leading oxidative species remain the same as that of in A6.26 system.

Base on the experimental results presented above, a possible mechanism for photocatalytic degradation of RhB over A6.26 and S6.26 can be conjectured (Scheme 1). Under the natural sunlight irradiation, the reaction starts with the excitation of the BiVO₄ photocatalysts, resulting in the promotion of electrons (e[−]) from the VB to the CB and the generation of holes (h⁺) in the VB. RhB adsorbed on the surface of BiVO₄ can directly be oxidized into degradation

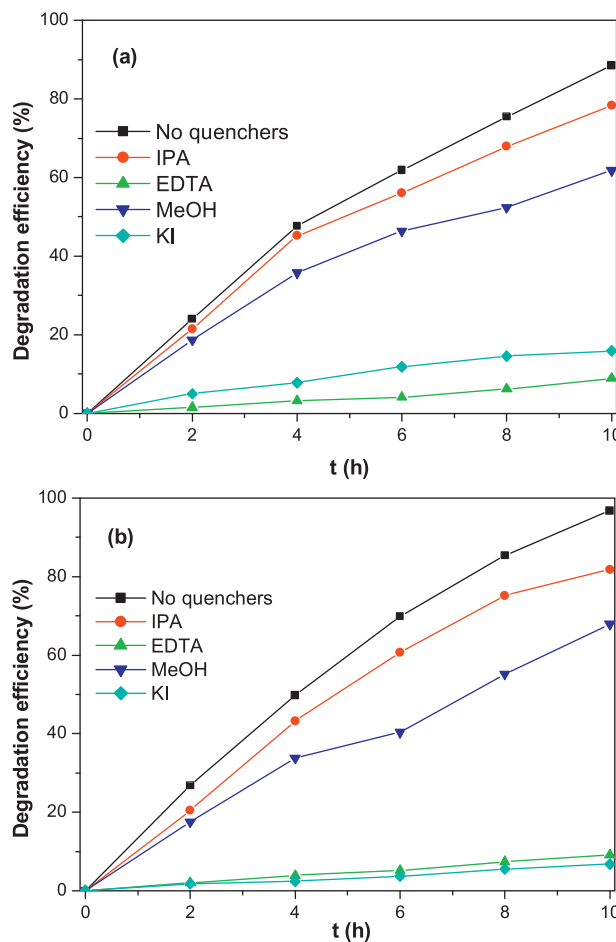
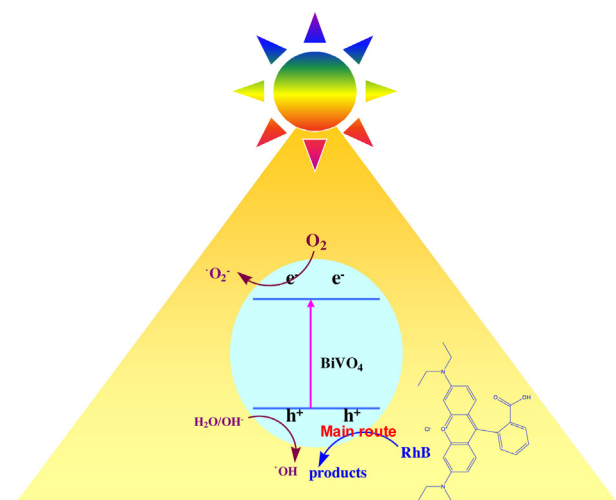


Fig. 11. Trapping experiments of photocatalytic degradation of RhB over (a) A6.26 and (b) S6.26 photocatalysts under natural sunlight irradiation with/without the presence of scavengers.

products by h^+ , which is regarded as the main degradation pathway in this reaction. Additionally, h^+ in the VB still have a few opportunity to react with OH^-/H_2O to form $\cdot OH$ radicals, and e^- in the CB might react with O_2 to produce $\cdot O_2^-$ radicals, the both of which play an assistant role in the natural sunlight-driven degradation of RhB.



Scheme 1. A speculated illustration for the photocatalytic degradation of RhB under natural sunlight irradiation over fabricated A6.26 and S6.26 photocatalysts.

3.5.2. Probing the effect of the morphological control of prepared BiVO4 hierarchical structures on their photocatalytic activities

Table S1 summarizes the surface, morphological, photochemical, and photocatalytic information of representative A-BiVO4 and S-BiVO4 samples based on the conducted characterization. In this regard, BET surface area has frequently been measured for investigating the possible effects on influencing the photocatalytic activities. In our study no apparent relationship can be found in Table S1 between the surface area of the photocatalysts and the corresponding photocatalytic activities, the observation of which is also confirmed by the plots in Fig. 12a and c, where the fluctuations of the specific reaction rate (on a surface area basis) are not influenced by the changes of surface area. This is in good agreement with the conclusions drawn in several of recent studies, which have indicated that surface area exerted no effect on the degradation efficiency of photocatalysts.

The pH-dictated hydrothermal synthesis herein brings about various shaped three-dimensional (3D) hierarchical BiVO4 structures. To seek the possible effects of the morphological control over the photocatalytic performance, discussion with regard to the aspect ratio of the fabricated structures would be meaningful. Interestingly, the photocatalytic efficiency is inversely proportional to the aspect ratio of the catalysts, as depicted in Fig. 12b (for A-BiVO4) and d (for S-BiVO4). This result is contrary to that of one-dimensional nanostructures reported in the literature [45,46].

The plots in terms of the photocatalytic reaction rates in Fig. 12a (for A-BiVO4) and c (for S-BiVO4) indicate that A6.26 and S6.26 possess the greatest capacity in photo-degradation of RhB. Combined with the discussion above, the effects of surface area and aspect ratio of the produced materials can be ruled out; the superior photocatalytic performances would be attributed to the perfect and stable shaped structures produced under specific hydrothermal conditions, which possess uniform size and shape distributions, namely, dumbbells for A6.26 and olives for S6.26. It is reasonable to speculate that the unique 3D shaped photocatalysts could promote the delocalization of photogenerated electrons and holes, therefore resulting in a suppression of e^-/h^+ recombination rates, and in consequence, an enhancement in the efficiency of photocatalytic degradation.

3.5.3. Testing the photocatalytic performances of prepared BiVO4 hierarchical structures with regard to the degradation of colorless sulfanilamide

Several previous studies have pointed out that colored pollutants such as dyes were not appropriate to act as model compounds for testing the visible-light-driven photocatalytic activity of photocatalysts due to dye sensitization [39,47]. To bypass this concern, we have selected sulfanilamide, a colorless, broadly-used, environment-concerned antibiotic as the degradation target in this investigation, where the visible-light-driven photocatalytic activities of both A6.26 and S6.26 were further evaluated by the degradation of sulfanilamide-contained wastewater under simulated sunlight irradiation. It can be observed in Fig. 13 that only approx. 13.1% sulfanilamide is degraded in a blank experiment without the presence of any BiVO4 photocatalysts (black curve). Accordingly, adding A6.26 into the system leads to the photodegradation of sulfanilamide, with a degradation efficiency of 53.6% within one hour (red curve in Fig. 13). Likewise, in the presence of S6.26, the degradation efficiency of sulfanilamide can reach up to 57.9% within applying 60 min simulated sunlight irradiation (blue curve in Fig. 13). Furthermore, the photocatalytic capacities of either A6.26 or S6.26 have not exhibited any significant loss after five cycling runs of photodegradation of sulfanilamide (data not shown). This investigation indicates that both A6.26 and S6.26

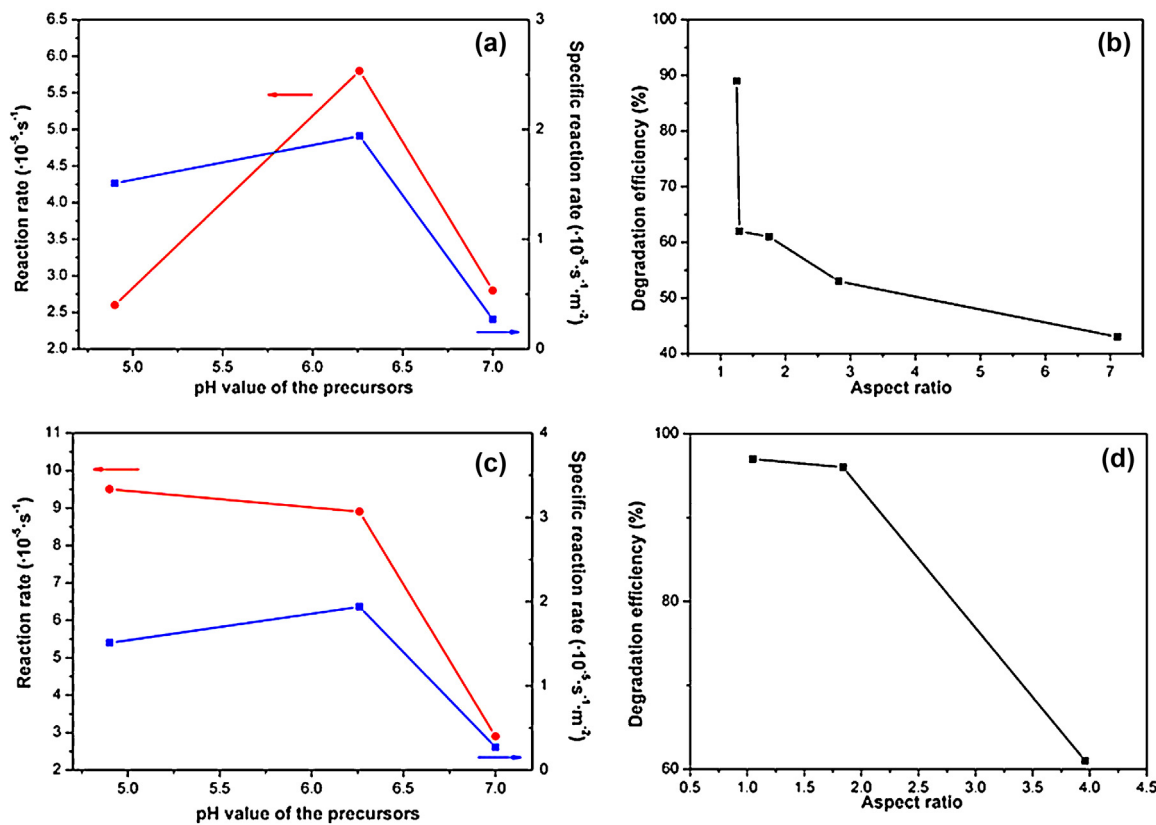


Fig. 12. RhB photodegradation reaction rates and specific reaction rates (per surface area unit) for (a) A-BiVO₄ and (c) S-BiVO₄ photocatalysts; Effects of aspect ratios of (b) A-BiVO₄ and (d) S-BiVO₄ hierarchical structures on the corresponding photodegradation performances.

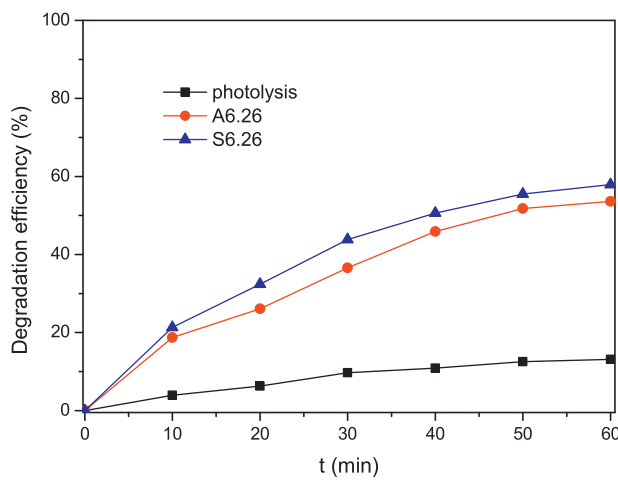


Fig. 13. Photocatalytic degradation of sulfanilamide under simulated sunlight irradiation by (a) A6.26 and (b) S6.26. (For interpretation of the references to color in this figure legend, the reader is referred to the web version of this article.)

possess good photocatalytic performances toward sulfanilamide degradation under visible light irradiation.

4. Conclusions

In summary, we have performed a first-time detailed study on the shape control of BiVO₄ hierarchical structures, as well as on the natural sunlight-driven photocatalytic activity of these synthesized materials. To this end, a time-saving, cost-effective, surfactant-free

approach for the controlled synthesis of uniform BiVO₄ hierarchical structures has been developed. Diverse BiVO₄ architectures, including peanuts, dumbbells, flowers, spheres, olives, and rod-sheaves, have been fabricated under facile pH-dictated low temperature hydrothermal processes. The influences of the morphologies of the synthesized BiVO₄ hierarchical structures on the photocatalytic degradation of Rhodamine B (RhB) have been investigated, indicating that the enhanced photocatalytic performance was not related to the surface area values and aspect ratios of the fabricated photocatalysts, but associated with the unique shaped configurations (e.g. A6.26 and S6.26) produced under specific conditions. The effects of the active species involved in the photocatalytic process and the cycle-stability of the prepared BiVO₄ photocatalysts have also been examined. Our study will not only contribute to the fundamental understandings about the controlled synthesis and relevant photocatalytic responses of BiVO₄ hierarchical structures, but also offer valuable insights into the strategic developments of long-term-investigated BiVO₄ photocatalysts into the real environmental issues.

Acknowledgments

The authors are grateful for the financial support from the Basic Scientific and Technological Frontier Project of Henan Province, PR China (Grant no. 132330410138, 102300410098, and 122300410293), the Key Science and Technology Program of Henan Province, PR China (Grant no. 122102310486, and 132102210129). The authors also would like to thank the Innovation Scientists and Technicians Troop Construction Projects of Henan Province, and the Plan for Scientific Innovation Talent of Henan Province (Grant no. 134200510014).

Appendix A. Supplementary data

Supplementary data associated with this article can be found, in the online version, at <http://dx.doi.org/10.1016/j.apcatb.2014.01.059>.

References

- [1] A. Taebi, R.L. Droste, *J. Environ. Manage.* 88 (2008) 688.
- [2] M. Kallel, C. Belaid, R. Boussahel, M. Ksibi, A. Montiel, B. Elleuch, *J. Hazard. Mater.* 163 (2009) 550.
- [3] M. Zupanc, T. Kosjek, M. Petkovsek, M. Dular, B. Kompare, B. Sirok, Z. Blazeka, E. Heath, *Ultrason. Sonochem.* 20 (2013) 1104.
- [4] C. Li, T. Ahmed, M. Ma, T. Edvinsson, J. Zhu, *Appl. Catal., B* 138 (2013) 175.
- [5] X. Su, Y. Tian, Z. Sun, Y. Lu, Z. Li, *Biosens. Bioelectron.* 49 (2013) 92.
- [6] H.G. Yu, R. Liu, X.F. Wang, P. Wang, J.G. Yu, *Appl. Catal., B* 111–112 (2012) 326.
- [7] J.L. Hu, H.M. Li, C.J. Huang, M. Liu, X.Q. Qiu, *Appl. Catal., B* 142–143 (2013) 598.
- [8] A.K. Kole, C.S. Tiwary, P. Kumbhakar, *CrystEngComm* 15 (2013) 5515.
- [9] S. Obregon, G. Colon, *J. Mol. Catal. A: Chem.* 376 (2013) 40.
- [10] L. Zhang, D.R. Chen, X.L. Jiao, *J. Phys. Chem. B* 110 (2006) 2668.
- [11] H. Fan, D. Wang, L. Wang, H. Li, P. Wang, T. Jiang, T. Xie, *Appl. Surf. Sci.* 257 (2011) 7758.
- [12] M. Shang, W. Wang, J. Ren, S. Sun, L. Zhang, *CrystEngComm* 12 (2010) 1754.
- [13] M.N. Chong, B. Jin, C.W.K. Chow, C. Saint, *Water Res.* 44 (2010) 2997.
- [14] L.S. Wang, M.W. Xiao, X.J. Huang, Y.D. Wu, J. Hazard. Mater. 161 (2009) 49.
- [15] G. Li, D. Zhang, J.C. Yu, *Chem. Mater.* 20 (2008) 3983.
- [16] Y. Lu, Y.S. Luo, D.Z. Kong, D.Y. Zhang, Y.L. Jia, X.W. Zhang, *J. Solid State Chem.* 186 (2012) 255.
- [17] H. Li, G. Liu, X. Duan, *Mater. Chem. Phys.* 115 (2009) 9.
- [18] D. Ressnig, R. Kontic, G.R. Patzke, *Mater. Chem. Phys.* 135 (2012) 457.
- [19] S. Obregon, A. Caballero, G. Colon, *Appl. Catal., B* 117–118 (2012) 59.
- [20] G. Tan, L. Zhang, H. Ren, S. Wei, J. Huang, A. Xia, *ACS Appl. Mater. Interfaces* 5 (2013) 5186.
- [21] J. Yu, A. Kudo, *Adv. Funct. Mater.* 16 (2006) 2163.
- [22] H. Zhang, B.W. Darvell, *Acta Biomater.* 6 (2010) 3216.
- [23] Q. Gong, X. Qian, X. Ma, Z. Zhu, *Cryst. Growth Des.* 6 (2006) 1821.
- [24] A.A. Chernov, J.J. Deyoreo, L.N. Rashkovich, *J. Optoelectron. Adv. Mater.* 9 (2007) 1191.
- [25] L. Zhang, J. Long, W. Pan, S. Zhou, J. Zhu, Y. Zhao, X. Wang, G. Cao, *Mater. Chem. Phys.* 136 (2012) 897.
- [26] H. Jiang, H. Dai, X. Meng, K. Ji, L. Zhang, J. Deng, *Appl. Catal., B* 105 (2011) 326.
- [27] X.Y. Chen, Z.J. Zhang, S.W. Lee, *J. Solid State Chem.* 181 (2008) 166.
- [28] W. Yin, W. Wang, L. Zhou, S. Sun, L. Zhang, *J. Hazard. Mater.* 173 (2010) 194.
- [29] P. Madhusudan, J.R. Ran, J. Zhang, J.G. Yu, G. Liu, *Appl. Catal., B* 110 (2011) 286.
- [30] M. Gotic, S. Music, M. Ivanda, M. Soufek, S. Popovic, *J. Mol. Struct.* 744 (2005) 535.
- [31] J. Tang, H. Quan, J. Ye, *Chem. Mater.* 19 (2007) 116.
- [32] T. Yang, D. Xia, *J. Cryst. Growth* 311 (2009) 4505.
- [33] P.O. Graf, D.J.M. deVlieger, B.L. Mojet, L. Lefferts, *J. Catal.* 262 (2009) 181.
- [34] T.Y. Podlipskaya, A.I. Bulavchenko, L.A. Sheludyakova, *J. Struct. Chem.* 48 (2007) 236.
- [35] X. Zhang, X. Quan, S. Chen, Y. Zhang, *J. Hazard. Mater.* 177 (2010) 914.
- [36] B. Cheng, W. Wang, L. Shi, J. Zhang, J. Ran, H. Yu, *Int. J. Photoenergy* 2012 (2012) 1.
- [37] M. Shang, W. Wang, L. Zhou, S. Sun, W. Yin, *J. Hazard. Mater.* 172 (2009) 338.
- [38] Y. Fu, X. Sun, X. Wang, *Mater. Chem. Phys.* 131 (2011) 325.
- [39] B. Ohtani, *Chem. Lett.* 37 (2008) 216.
- [40] X. Qiu, L. Li, J. Zheng, J. Liu, X. Sun, G. Li, *J. Phys. Chem. C* 112 (2008) 12242.
- [41] S. Li, Z. Ma, J. Zhang, Y. Wu, Y. Gong, *Catal. Today* 139 (2008) 109.
- [42] M. Hojamberdiev, G. Zhu, Y. Xu, *Mater. Res. Bull.* 45 (2010) 1934.
- [43] H.N. Luitel, R. Chand, T. Torikai, M. Yada, T. Watari, *Int. J. Photoenergy* 2013 (2013) 1.
- [44] H.Q. Jiang, H. Endo, H. Natori, M. Nagai, K. Kobayashi, *Mater. Res. Bull.* 44 (2009) 700.
- [45] A. Leelavathi, G. Madras, N. Ravishankar, *Phys. Chem. Chem. Phys.* 15 (2013) 10795.
- [46] D. Zhang, G. Li, F. Wang, J.C. Yu, *CrystEngComm* 12 (2010) 1759.
- [47] X. Yan, T. Ohno, K. Nishijima, R. Abe, B. Ohtani, *Chem. Phys. Lett.* 429 (2006) 606.